We are IntechOpen, the world's leading publisher of Open Access books
Built by scientists, for scientists

6,900
Open access books available

185,000
International authors and editors

200M
Downloads

Our authors are among the

154
Countries delivered to

TOP 1%
most cited scientists

12.2%
Contributors from top 500 universities

WEB OF SCIENCE™

Selection of our books indexed in the Book Citation Index in Web of Science™ Core Collection (BKCI)

Interested in publishing with us?
Contact book.department@intechopen.com

Numbers displayed above are based on latest data collected.
For more information visit www.intechopen.com

Chapter 5

A Comprehensive Model of the Transport Phenomena in Gas Metal Arc Welding

Junling Hu, Zhenghua Rao and Hai-Lung Tsai

Additional information is available at the end of the chapter

http://dx.doi.org/10.5772/64160

Abstract

A comprehensive two-dimensional gas metal arc welding (GMAW) model was developed to take into account all the interactive events in the gas metal arc welding process, including the arc plasma, melting of the electrode, droplet formation, detachment, transfer, and impingement onto the workpiece, and the weld-pool dynamics and weld formation. The comprehensive GMAW model tracks the free surface using the volume of fluid method and directly modeled the coupling effects between the arc domain and the metal domain, thus eliminating the need to assign boundary conditions at the interface. A thorough investigation of the plasma arc characteristics was conducted to study its effects on the dynamic process of droplet formation, detachment, impingement, and weld-pool formation. It was found that the droplet transfer and the deformed electrode and weld-pool surfaces significantly influence the transient distributions of current density, arc temperature, and arc pressure, which in turn affect the droplet formation, droplet transfer, and weld-pool dynamics.

Keywords: GMAW, arc plasma, weld-pool dynamics, metal transfer, droplet formation

1. Introduction

Gas metal arc welding (GMAW) is the most widely used joining process due to its ability to provide high-quality welds for a wide range of ferrous and non-ferrous alloys at low cost and high speed. As shown in **Figure 1**, GMAW is an arc-welding process that uses arc plasma between a continuously fed filler metal electrode and the workpiece to melt the electrode and the workpiece. The melted filler metal forms droplets and deposits on the partially melted

INTECH
open science | open minds

© 2016 The Author(s). Licensee InTech. This chapter is distributed under the terms of the Creative Commons Attribution License (http://creativecommons.org/licenses/by/3.0), which permits unrestricted use, distribution, and reproduction in any medium, provided the original work is properly cited. CC BY

workpiece to form a weld pool. The weld pool solidifies to bond the workpieces after the arc moves away. A shielding gas is fed through the gas nozzle to protect the molten metal from nitrogen and oxygen in the air. GMAW is also commonly known as metal inert gas (MIG) since inert gasses argon and helium are often used as a shielding gas. An active shielding gas containing oxygen and carbon dioxide is also used and thus the GMAW process is also called metal active gas (MAG). Direct current is usually used with the filler wire as the anode electrode to increase wire melting rate. GMAW can be easily adapted for high-speed robotic, hard automation, and semiautomatic welding applications.

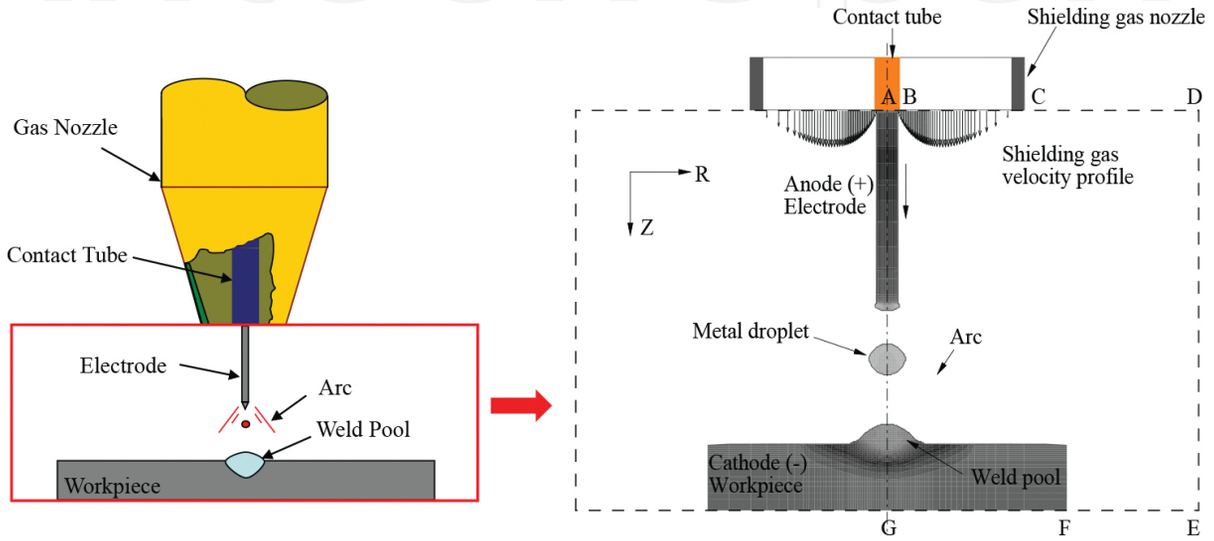

Figure 1. Schematic representation of a GMAW system with the computational domain shown inside the frame.

GMAW is a complex process with three major coupling events: (1) the evolution of arc plasma, (2) the dynamic process of droplet formation, detachment, and impingement onto the weld pool, and (3) the dynamics of the welding pool under the influences of the arc plasma and the periodical impingement of droplets. The stability of the GMAW process and the weld quality depend on many process parameters, such as welding current, welding voltage, wire feed speed, wire material and wire size, arc length, contact tube to workpiece distance, workpiece material and thickness, shielding gas properties, shielding gas flow rate, welding speed, etc. Selection of these welding-processing parameters relies on extensive experimentation and is an expensive trial-and-error process. Therefore, tremendous research efforts have been devoted to developing mathematical models of the GMAW process in order to reveal the underlying welding physics and provide key insights of process parameters for process optimization and defect prevention. Due to the complexity of the welding process and the associated numerical difficulty, many numerical models in the literature have simplified the GMAW process and only focused on one or two events. Many works on droplet formation [1–8] and weld-pool dynamics [9–29] have not included the arc plasma. More works now have been devoted to study the arc plasma and its influence on the metal transfer [30–41] and weld-pool dynamics [41–49].

http://dx.doi.org/10.5772/64160

In these simplified models, the droplet formation is considered as an isolated process in the electrode. The influence of the arc plasma is considered as boundary conditions with assumed distributions, such as linear current density distributions [1–3] or Gaussian distributions for the current density and heat flux [6–8].

The effects of droplet impingement on the weld pool have been significantly simplified as boundary conditions in the modeling of the weld-pool dynamics by many researchers [9–21]. The weld-pool surface was assumed to be flat [9–14] or modeled with boundary-fitted coordinates [13–15]. The dynamic impingement of a droplet onto the weld pool has been omitted [13], treated as a liquid column [14] or cylindrical volumetric heat source [15–19] acting on the weld pool in many weld-pool models. Only recent models [20–29] have simulated the dynamic interaction of droplets impinging onto the weld pool including both heat transfer and fluid flow effects and tracked the deformed weld pool free surface. However, they all applied assumed current, heat flux, and arc pressure boundary conditions at the weld-pool surface and also approximated the droplet impingement with the assumed droplet shape, volume and temperature, and impinging frequency and velocity.

In almost all aforementioned studies, the interaction of arc plasma with electrode melting, droplet generation and transfer, and weld-pool dynamics was not considered. Linear or Gaussian current density and heat flux were assumed as boundary conditions at the electrode surface [1–6] and weld-pool surface [15–29]. However, the surface of the workpiece is highly deformable, and the profile of the electrode changes rapidly, which greatly influence the arc plasma flow and thus change the current, heat flux, and momentum distribution at the surfaces of electrode and workpiece. Furthermore, the arc plasma can be dramatically distorted when there are free droplets between the electrode tip and the surface of the weld pool as observed in experimental studies [30–32]. Several models [33–39] have been developed to study the dynamic interaction of the arc plasma with the droplet formation. However, the droplet was eliminated when it was detached from the electrode tip or when it reaches the workpiece. The weld-pool dynamics was also omitted and the workpiece was treated as a flat plate. Some recent models [40–43] included the arc plasma, the filler wire, and the workpiece to study the direct interactions of the three domains. However, they are not completely coupled models since the droplet transfer in the arc still relies on an empirical formulation to calculate the plasma drag force in [43] or the droplet impingement is not simulated in [40–42].

The authors developed a fully coupled comprehensive GMAW model [44–52] to include the entire welding process—the arc plasma evolution, the electrode melting, the droplet formation and detachment, the droplet transfer in the arc, the droplet impingement onto the weld pool, and the weld-pool dynamics and solidification. The volume of fluid (VOF) technique was used to track the interface of the arc plasma and the metal. The temperature, pressure, velocity, electric, and magnetic fields are calculated in the entire computational domain, including the arc, filler wire, and the workpiece without using assumed heat, current, and pressure distributions at the interfaces. In the following sections, the comprehensive mathematical model is first presented to model the GMAW physics, and then the computational results are presented to show the evolution of the arc plasma and its dynamic interaction with the droplet formation, detachment, transfer, and impingement, and the weld-pool dynamics.

2. Mathematical model

2.1. Governing equations

The computational domain is shown in **Figure 1**, which has an anode region, an arc region, and a cathode region. The governing equations for the arc, the electrode, and the workpiece can be written in a single set based on the continuum formulation given by Diao and Tsai [53]:

Mass continuity

$$\frac{\partial}{\partial t}(\rho)+\nabla\cdot(\rho \boldsymbol{V})=0 \tag{1}$$

Momentum

$$\begin{aligned}&\frac{\partial}{\partial t}(\rho u)+\nabla\cdot(\rho \boldsymbol{V} u)=\nabla\cdot(\mu_l\frac{\rho}{\rho_l}\nabla u)-\frac{\partial p}{\partial r}-\frac{\mu_l}{K}\frac{\rho}{\rho_l}(u-u_s)-\frac{C\rho^2}{K^{1/2}\rho_l}|u-u_s|(u-u_s)\\&-\nabla\cdot(\rho f_s f_l \boldsymbol{V}_r u_r)-J_z\times B_\theta\end{aligned} \tag{2}$$

$$\begin{aligned}&\frac{\partial}{\partial t}(\rho v)+\nabla\cdot(\rho \boldsymbol{V} v)=\nabla\cdot(\mu_l\frac{\rho}{\rho_l}\nabla v)-\frac{\partial p}{\partial z}-\frac{\mu_l}{K}\frac{\rho}{\rho_l}(v-v_s)-\frac{C\rho^2}{K^{1/2}\rho_l}|v-v_s|(v-v_s)\\&-\nabla\cdot(\rho f_s f_l \boldsymbol{V}_r v_r)+\rho g\beta_T(T-T_0)+J_r\times B_\theta\end{aligned} \tag{3}$$

where $\boldsymbol{V}$ is the velocity vector, and u and v are the velocities in the r and z directions, respectively; $\boldsymbol{V}_r$ is the relative velocity vector between the liquid phase and the solid phase. The subscripts s and l refer to the solid and liquid phases, respectively, and the subscript 0 represents the initial condition. g is the gravitational acceleration, p is the pressure, ρ is the density, μ is the viscosity, β_T is the thermal expansion coefficient, T is the temperature, J_r and J_z are current densities in the respective r and z directions and B_θ is the self-induced electromagnetic field. K is the permeability function, C is the inertial coefficient, and f is the mass fraction.

Energy

$$\begin{aligned}&\frac{\partial}{\partial t}(\rho h)+\nabla\cdot(\rho \boldsymbol{V} h)=\nabla\cdot(\frac{k}{c_s}\nabla h)+\nabla\cdot(\frac{k}{c_s}\nabla(h_s-h))-\nabla\cdot(\rho(\boldsymbol{V}-\boldsymbol{V}_s)(h_l-h))\\&-\Delta H\frac{\partial f_l}{\partial t}+\frac{J_r^2+J_z^2}{\sigma_e}-S_R+\frac{5k_b}{e}(\frac{J_r}{c_s}\frac{\partial h}{\partial r}+\frac{J_z}{c_s}\frac{\partial h}{\partial z})\end{aligned} \tag{4}$$

http://dx.doi.org/10.5772/64160

where h is the enthalpy, k is the thermal conductivity, c is the specific heat, S_R is the radiation heat loss, k_b is the Stefan-Boltzmann constant, σ_e is the electrical conductivity, and e is the electronic charge.

Current continuity

$$\nabla^2\phi = \frac{1}{r}\frac{\partial}{\partial r}\left(r\frac{\partial\phi}{\partial r}\right) + \frac{\partial^2\phi}{\partial z^2} = 0 \tag{5}$$

Ohm's law

$$J_r = -\sigma_e\frac{\partial\phi}{\partial r},\ J_z = -\sigma_e\frac{\partial\phi}{\partial z} \tag{6}$$

Maxwell's equation

$$B_\theta = \frac{\mu_0}{r}\int_0^r J_z r dr \tag{7}$$

where ϕ is the electrical potential and μ_0 is the magnetic permeability.

The continuum model [53] included the first- and second-order drag forces and the interaction between the solid and liquid phases due to the relative velocity in the mushy zone ($0< f_l <1$ and $0< f_s <1$), which are represented by the corresponding third to fifth terms in the right-hand side of Eqs. (2) and (3). The energy flux due to the relative phase motion in the mushy zone is represented as the second term in the right-hand side of Eq. (4). The enthalpy method is used for phase change during the fusion and solidification processes. The enthalpy for the solid and liquid phases can be expressed as

$$h_s = c_s T,\ h_l = c_l T + (c_s - c_l)T_s + H \tag{8}$$

where H is the latent heat of fusion.

Continuum density (ρ), specific heat (c), thermal conductivity (k), velocity ($\boldsymbol{V}$), and enthalpy (h) are defined as follows:

$$\rho = \rho_s g_s + \rho_l g_l,\ c = f_s c_s + f_l c_l,\ k = k_s g_s + k_l g_l$$

$$f_l = \frac{\rho_s g_s}{\rho},\quad f_s = \frac{\rho_l g_l}{\rho} \tag{9}$$

$$\boldsymbol{V} = f_s \boldsymbol{V}_s + f_l \boldsymbol{V}_l, \quad h = f_s h_s + f_l h_l$$

where g is the volume fraction of the solid or liquid phase.

The permeability function is assumed to be analogous to fluid flow in porous media employing the Carman-Kozeny equation [54, 55]

$$K = \frac{g_l^3}{c_1 (1 - g_l)^2}, \quad c_1 = \frac{180}{d^2} \tag{10}$$

where d is proportional to the dendrite dimension. In this study, it is assumed to be a constant and is on the order of 10^{-2} cm.

The inertial coefficient, C, is calculated from [56]

$$C = 0.13 g_l^{-3/2} \tag{11}$$

2.2. Arc region

The arc region includes the arc plasma column and the surrounding shielding gas. The arc plasma is assumed to be in local thermodynamic equilibrium (LTE) [57]. The plasma properties, including enthalpy, density, viscosity, specific heat, thermal conductivity, and electrical conductivity, are calculated from an equilibrium composition [57, 58]. The influence of metal vapor on plasma material properties [37–42] is not considered in the present study. The plasma is also assumed to be optically thin, thus the radiation may be modeled as a radiation heat loss per unit volume represented by S_R in Eq. (4) [57, 58].

2.3. Metal region and tracking of free surfaces

The metal region includes the electrode, droplet in the arc, and the workpiece. The dynamic evolution of the droplet formation of the electrode tip, the droplet transfer in the arc, and the weld-pool dynamics require precise tracking of the free surface of the metal region. The volume of fluid method is used to track the moving free surface [59]. A volume of fluid function, $F(r,z,t)$, is used to track the location of the free surface. This function represents the volume of fluid per unit volume and satisfies the following equation:

$$\frac{dF}{dt} = \frac{\partial F}{\partial t} + (\boldsymbol{V} \cdot \nabla) F = 0 \tag{12}$$

The average value of F in a cell is equal to the volume fraction of the cell occupied by the metal. A zero value of F indicates that a cell contains no metal, whereas a unit value indicates that the cell is full of metal. Cells with F values between zero and one are partially filled with metal.

http://dx.doi.org/10.5772/64160

2.4. Forces at the interface of the arc plasma and metal regions

The molten metal is subject to body forces and surfaces forces at the interface of the arc plasma and metal regions. The body forces include gravity, buoyancy force, and electromagnetic force. The surface forces include arc plasma shear stress, arc pressure, surface tension due to surface curvature, and Marangoni shear stress due to temperature difference. The surface forces are included as source terms to the momentum equations according to the CSF (continuum surface force) model [59–61]. Using F of the VOF function as the characteristic function, the surface forces are transformed to the localized body forces and added in the free surface cells.

The arc plasma shear stress is calculated from the velocities of the arc plasma cells at the free surface

$$\vec{\tau}_{ps} = \mu \frac{\partial \mathbf{V}}{\partial \vec{s}} \tag{13}$$

where μ is the viscosity of the arc plasma. The arc pressure at the metal surface is also obtained from the results in the arc region.

Surface tension pressure is normal to the free surface and can be expressed as [60]

$$p_s = \gamma \kappa \tag{14}$$

where γ is the surface tension coefficient. The free surface curvature κ is given by

$$\kappa = -\left[\nabla \cdot \left(\frac{\vec{n}}{|\vec{n}|}\right)\right] = \frac{1}{|\vec{n}|}\left[\left(\frac{\vec{n}}{|\vec{n}|} \cdot \nabla\right)|\vec{n}| - (\nabla \cdot \vec{n})\right] \tag{15}$$

where $\vec{n}$ is the surface normal, calculated as the gradient of the VOF function

$$\vec{n} = \nabla F \tag{16}$$

The temperature-dependent Marangoni shear stress is in a direction tangential to the local free surface and is given by [7]

$$\vec{\tau}_{Ms} = \frac{\partial \gamma}{\partial T}\frac{\partial T}{\partial \vec{s}} \tag{17}$$

where $\vec{s}$ is a tangent vector of the local free surface.

2.5. Energy terms at the interface of the arc plasma and metal regions

2.5.1. Plasma-anode interface

The anode sheath region at the plasma-electrode interface is a very thin region, about 0.02-mm thick [57], and is at nonlocal thermal equilibrium. The very thin region is treated as a special interface by adding energy source terms, S_a in the metal region and S_{ap} in the arc region:

$$S_a = \frac{k_{eff}(T_{arc} - T_a)}{\delta} + J_a \phi_w - \varepsilon k_b T_a^4 - q_{ev} H_{ev} \tag{18}$$

$$S_{ap} = -\frac{k_{eff}(T_{arc} - T_a)}{\delta} \tag{19}$$

where T_{arc} and T_a are the respective arc plasma and metal temperature at the plasma-anode interface, k_{eff} is the harmonic mean of the thermal conductivities of the arc plasma and the anode materials, δ is the thickness of the anode sheath region and is taken as 0.1 mm according to the maximum thickness observed by experiments [62], ϕ_w is the work function of the anode material, J_a is the anode current calculated as the square root of J_r^2 and J_z^2, ε is the metal surface emissivity and k_b is the Stefan-Boltzmann constant, H_{ev} is the latent heat of vaporization of metal vapor, and q_{ev} is the mass rate of evaporation at the metal surface. The mass rate of evaporation of metal, q_{ev} for steel can be expressed as [63]

$$\log(q_{ev}) = A_v + \log P_{atm} - 0.5 \log T \tag{20}$$

$$\log P_{atm} = 6.121 - \frac{18836}{T} \tag{21}$$

The four terms in Eq. (18) take into account thermal conduction, electron heating associated with the work function of the anode material, black-body radiation heat loss, and evaporation heat loss, respectively, at the metal surface. The energy equation for the plasma region only considers the cooling effects through conduction.

http://dx.doi.org/10.5772/64160

2.5.2. Plasma-cathode interface

Similarly, energy source terms S_c and S_{cp} are added to the corresponding metal and arc regions at the plasma-cathode interface, taken into account the conduction, radiation, and evaporation terms:

$$S_c = \frac{k_{eff}(T_{arc} - T_c)}{\delta} - q_{ev}H_{ev} - \varepsilon k_b T_c^4 \tag{22}$$

$$S_{cp} = -\frac{k_{eff}(T_{arc} - T_c)}{\delta} \tag{23}$$

where T_c is the metal surface temperature at the cathode surface, k_{eff} is the harmonic mean of the thermal conductivities of the arc plasma and the cathode materials, and δ is the thickness of the cathode and is taken as 0.1 mm.

2.6. External boundary conditions

The computational domain for a two-dimensional (2D) axisymmetric GMAW system is shown as ABCDEFGA in **Figure 1**. The external boundary conditions are listed in **Table 1**. Symmetrical boundary condition is assigned along the centerline AG.

	AB	BC	CD	DE	EF	FG	GA
u	0	0	0	$\frac{\partial(\rho u)}{\partial r}=0$	0	0	0
v	v_w	Eq. (24)	$\frac{\partial(\rho v)}{\partial z}=0$	0	0	0	$\frac{\partial v}{\partial r}=0$
h	T = 300 K	T = 300 K	T = 300 K	T = 300 K	T = 300 K	T = 300 K	$\frac{\partial T}{\partial r}=0$
ϕ	$-\sigma\frac{\partial\phi}{\partial z}=\frac{I}{\pi R_c^2}$	$\frac{\partial\phi}{\partial z}=0$	$\frac{\partial\phi}{\partial z}=0$	$\frac{\partial\phi}{\partial r}=0$	$\phi=0$	$\phi=0$	$\frac{\partial\phi}{\partial r}=0$

Table 1. Boundary conditions on the outer boundaries.

The velocity boundary takes into account the wire feed rate at AB, shielding gas inlet at BC, open boundaries at CD and DE, and non-slip wall condition at EF. The inflow of shielding gas from the nozzle at BC is represented by a fully developed axial velocity profile for laminar flow in a concentric annulus [64]:

$$v(r) = -\frac{2Q}{\pi}\frac{R_n^2 - r^2 + (R_n^2 - R_w^2)\dfrac{\ln(r/R_n)}{\ln(R_n/R_w)}}{R_n^4 - R_w^4 + \dfrac{(R_n^2 - R_w^2)^2}{\ln(R_n/R_w)}} + V_w\frac{\ln(R_n/r)}{\ln(R_n/R_w)} \tag{24}$$

where Q is the shielding gas flow rate, V_w is the wire feed rate, R_w and R_n are the radius of the electrode and the internal radius of the shielding gas nozzle, respectively.

The temperature boundaries along AD, DE, and EG are set as the room temperature. The boundary conditions for current flow include a zero voltage at the bottom of the workpiece FG, uniform current density along AB specified as $J_z = -\sigma_e\frac{\partial\phi}{\partial z} = \frac{I}{\pi R_w^2}$, and zero current flow along the other surfaces.

3. Numerical methods

At each time step, the calculation involves separate calculations in the arc region and the metal region, the coupling of the two regions through the interface boundary conditions described in Sections 2.4 and 2.5, and updating the arc and metal regions after obtaining the new free surface using the VOF method, Eq. (12), in the metal region.

The arc plasma region uses a fully implicit formulation and an upwind scheme for the combined convection/diffusion coefficients, and the SIMPLE algorithm [65] for the velocity and temperature fields. The metal region uses the method developed by Torrey et al. [59] to calculate the velocity and temperature fields.

The computational domain is 5 cm in radius and 3.04 cm in length. A nonuniform grid system is used with finer meshes near the electrode tip, in the arc column and the weld pool, where a fine mesh of 0.01 cm is used. Time step size is set as 5×10^{-6} s for a stable numerical solution.

4. Results and discussion

In this chapter, the comprehensive model [44, 45] is used to simulate a spot GMAW welding of a mild steel workpiece with a mild steel electrode under a constant current of 220 A shielded by argon. The electrode has a diameter of 0.16 cm and the workpiece is a mild steel disk with a 3-cm diameter and a 0.5-cm thickness. The contact tube is set flush with the bottom of the gas nozzle and has a contact tube to workpiece distance of 2.54 cm. The wire feed rate is 4.5 cm/s and the initial arc length is 0.8 cm. The shielding gas flow rate is 24 l/min and the inner diameter of the nozzle is 1.91 cm.

The temperature-dependent material properties of argon and the radiation loss term (SR) in Eq. (4) are taken from [58] and are plotted in **Figure 2**. **Table 2** lists the properties of

http://dx.doi.org/10.5772/64160

the solid and liquid mild steel taken from [7] and other parameters used in the computation.

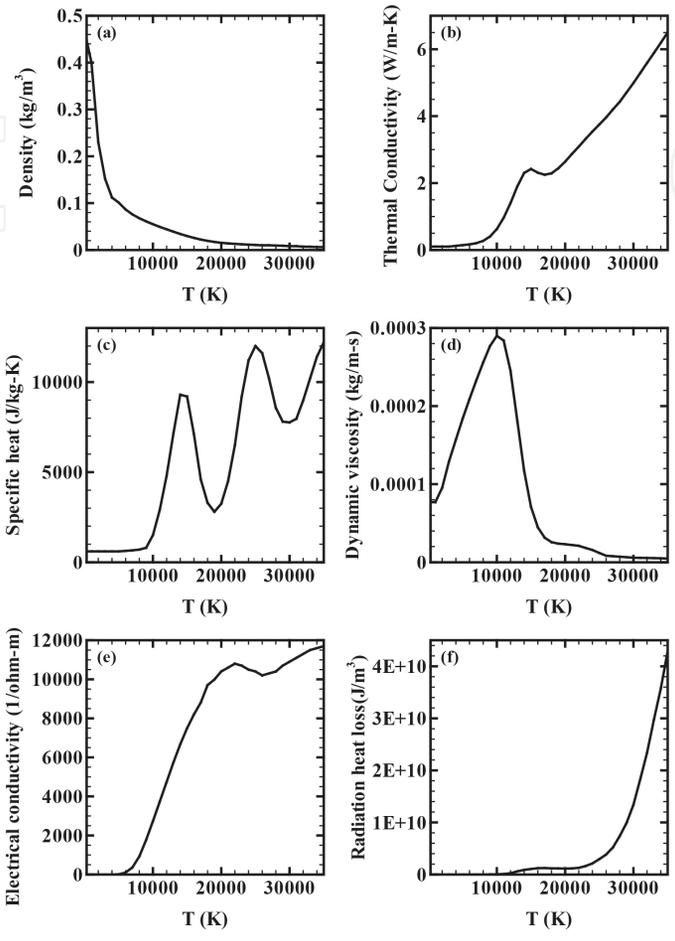

Figure 2. Temperature-dependent material properties of argon and the volume radiation heat loss taken from [58].

Nomenclature	Symbol	Value (unit)
Constant in Eq. (20)	A_v	2.52
Specific heat of solid phase	c_s	700 (J kg^{-1} K^{-1})
Specific heat of liquid phase	c_l	780 (J kg^{-1} K^{-1})
Thermal conductivity of solid phase	k_s	22 (W m^{-1} K^{-1})
Thermal conductivity of liquid phase	k_l	22 (W m^{-1} K^{-1})
Density of solid phase	ρ_s	7200 (kg m^{-3})
Density of liquid phase	ρ_l	7200 (kg m^{-3})
Thermal expansion coefficient	β_T	4.95×10^{-5} (K^{-1})
Radiation emissivity	ε	0.4
Dynamic viscosity	μ_l	0.006 (kg m^{-1} s^{-1})
Latent heat of fusion	H	2.47×10^5 (J kg^{-1})

Nomenclature	Symbol	Value (unit)
Latent heat of vaporization	H_{ev}	7.34×10^{6} (J kg^{-1})
Solidus temperature	T_s	1750 (K)
Liquidus temperature	T_l	1800 (K)
Ambient temperature	T_∞	300 (K)
Vaporization temperature	T_{ev}	3080 (K)
Surface tension coefficient	γ	1.2 (N m^{-1})
Surface tension temperature gradient	$\partial\gamma/\partial T$	10^{-4} (N m^{-1} K^{-1})
Work function	ϕ_w	4.3 V
Electrical conductivity	σ_e	7.7×10^{5} (Ω^{-1}m^{-1})

Table 2. Thermophysical properties of mild steel and other parameters.

4.1. Arc plasma evolution

Figure 3 shows the distributions of arc plasma temperature and pressure before and after the first droplet is detached and transferred to the workpiece. The shape of the electrode and workpiece are marked with thick lines. At t = 100 ms, the first droplet is formed at the electrode tip and the workpiece is still flat before a weld pool is formed. The arc shown in **Figure 3(a)** has a bell-shaped envelope with a maximum temperature of 19,300 K underneath the droplet. The high-temperature arc covers the droplet and expands as it moves toward the workpiece. The arc pressure contours at t = 100 ms in **Figure 3(b)** has two high-pressure regions. One is underneath the droplet caused by the pinch effect of the electromagnetic force, and the other is near the workpiece due to the stagnation of the plasma flow impinging onto the workpiece. The velocity field and streamlines in **Figure 4** show that shielding gas flows downward from the gas nozzle along the electrode surface and then is drawn to the electrode around the electrode tip. The ionized shielding gas around the electrode tip is pinched by the radially

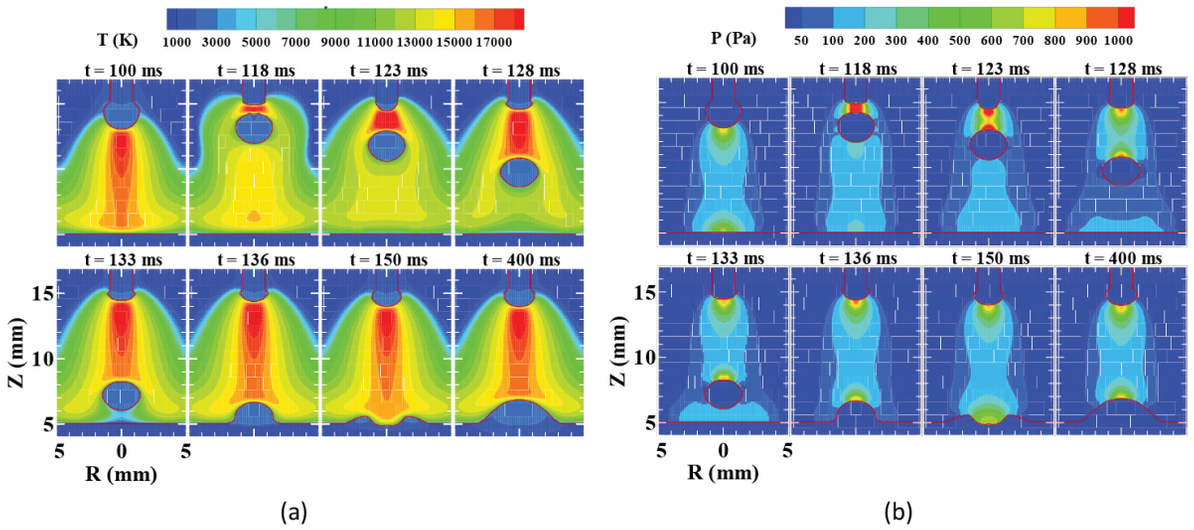

Figure 3. Arc plasma evolution during the first droplet formation, detachment, transfer, and impingement onto the workpiece: (a) temperature distributions in the arc plasma and (b) pressure distributions in the arc plasma.

http://dx.doi.org/10.5772/64160

inward and axially downward electromagnetic force toward the workpiece. The maximum axial velocity in the arc column is found to be 230 m/s on the axis. The corresponding current density distribution in **Figure 5** clearly shows that current diverges from the electrode tip and converges at the cathode in the workpiece, which results in inward and downward electromagnetic forces around the droplet and the inward and upward electromagnetic forces near the workpiece.

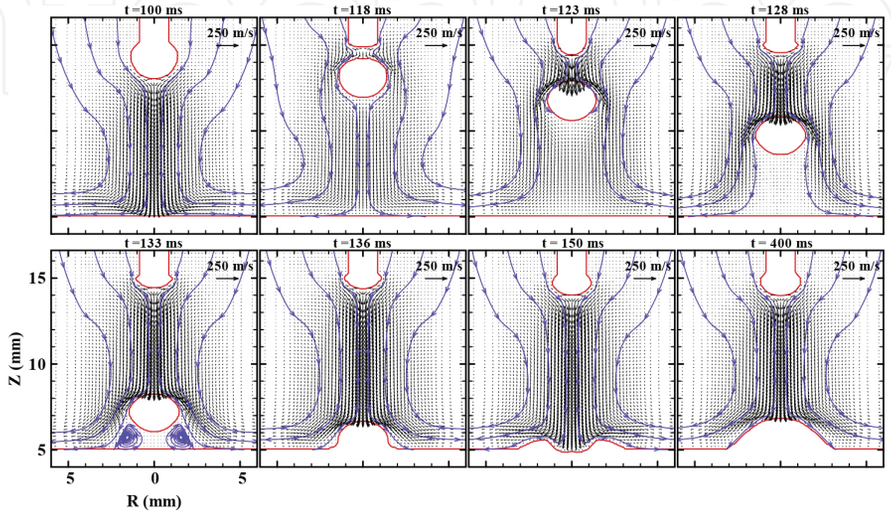

Figure 4. The corresponding velocity distributions in the arc plasma for the cases shown in **Figure 3**.

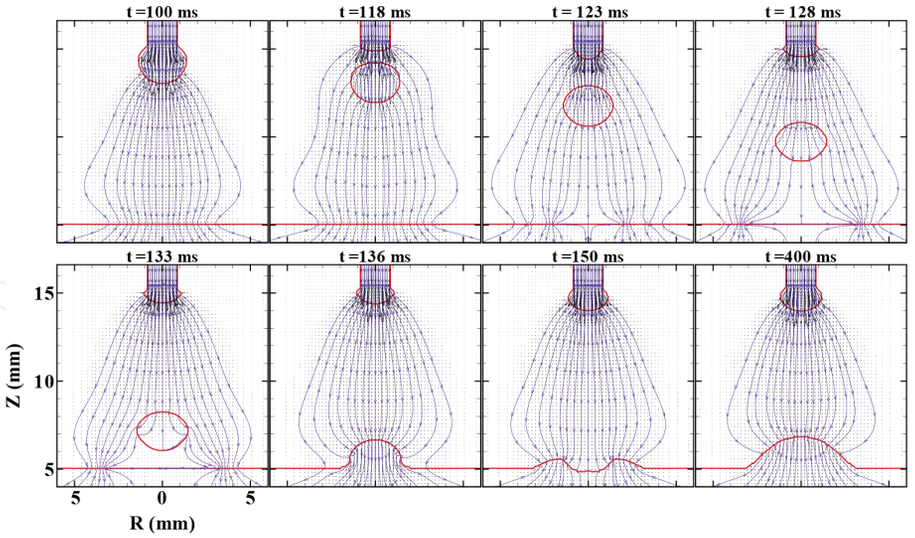

Figure 5. The corresponding current distributions in the arc plasma for the cases shown in **Figure 3**.

After the droplet is detached from the electrode at t = 118 ms, a new arc plasma is struck between the electrode tip and the top surface of the detached droplet. During the transfer of the detached droplet to the workpiece, the existence of the moving droplet greatly distorts the arc shape and flow pattern. Between t = 118 and 133 ms, current flow through the moving

droplet decreases and the temperature of the arc plasma underneath the droplet also decreases. The arc plasma above the droplet is driven by the electromagnetic force and accelerates above the electrode. The high-velocity arc plasma flow impinges onto the top surface of the relatively slow-moving droplet and then flows around it. The flow pattern of the arc plasma around the droplet is similar to a flow around a sphere, including a high-pressure region formed at the droplet top surface due to the impingement and a low-pressure wake region below the droplet. The pressure drag is the main driving force for the droplet acceleration in the arc plasma. These arc plasma transport phenomena are confirmed by the experimental results of [30–32], but are significantly different from the numerical results in [43]. The unified GMAW model in [43] predicted current tended to flow through the detached droplet and a strong arc plasma flow formed beneath the droplet. However, the flow pattern in [43] failed to push the detached droplet downward in the arc plasma and thus an empirical equation was used to calculate the arc plasma drag force.

The first droplet reaches the workpiece around t = 136 ms, and a weld pool with an oscillating surface forms at the workpiece. The current distribution at the workpiece is greatly influenced by the weld-pool surface shape. The current tends to converge on the projected area at the workpiece, which may be at the workpiece center as in the cases of both t = 136 and 400 ms or not at the center as that of t = 150 ms.

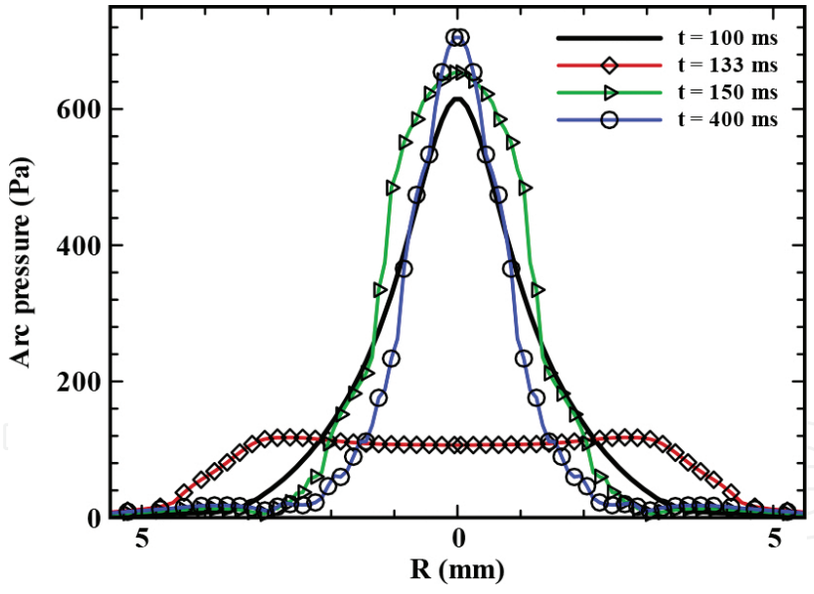

Figure 6. Arc pressure distributions along the radial direction at the workpiece surface.

In many of the weld-pool models [7–29], the arc pressure distribution at the center of the workpiece surface was assumed to be a Gaussian distribution with a fixed amplitude and distribution radius. However, the arc pressure distribution at the workpiece surface changes dramatically during the welding process as shown in **Figure 6**. Both the magnitude and distribution region varies with the evolution of the electrode and weld-pool surfaces and the presence of the detached droplet. Low arc pressure with a flat-top distribution is found at the

http://dx.doi.org/10.5772/64160

weld-pool surface at t = 133 ms when there is a detached droplet in the arc column, whereas high and concentrated arc pressure distribution is observed at t = 400 s when the weld-pool surface is projected and the arc column has no detached droplet. These distributions significantly deviate from the assumed Gaussian distribution in many weld-pool models [7–29]. Similarly, their assumed Gaussian distributions of current and heat flux cannot represent the dynamic boundary conditions at the weld-pool surface.

4.2. Droplet formation and transfer

Droplet formation is determined by the concentrated heating due to the recombining electrons at the electrode surface and the flow pattern within the droplet caused by a balance of forces acting on the droplet, which includes electromagnetic force, surface tension force, gravity, arc pressure, and plasma shear stress. To clearly illustrate the heat transfer and fluid flow within the droplet at the electrode tip, the distributions of temperature, velocity, electrical potential, current, and electromagnetic force within the droplet at t = 100 ms are drawn in **Figure 7**. A vortex flow forms in the droplet with a downward flow along the centerline and an upward flow at the surface. The fluid circulation enhances the mixing of cold fluid at the center with the hot surface fluid. The downward flow is caused by the inward and downward electromagnetic force at the upper part of the droplet near the melt line marked as a dashed line. The electromagnetic force and current density are determined by the electrical potential distribution. Current slightly diverges in the upper part of the droplet and converges in the lower part and then flows out of the droplet surface from the lower part of the droplet. The current flow pattern results in an electromagnetic force that is radially inward and axially downward at the upper part and upward at the bottom part. The upward electromagnetic force, surface tension, and arc pressure at the droplet bottom change the fluid to flow upward along the surface. At the balance of electrons heating, arc plasma heating, evaporation and radiation cooling, and convection cooling, the maximum temperature at the droplet surface is found to be 2936 K, which is close to the experimental result of [58].

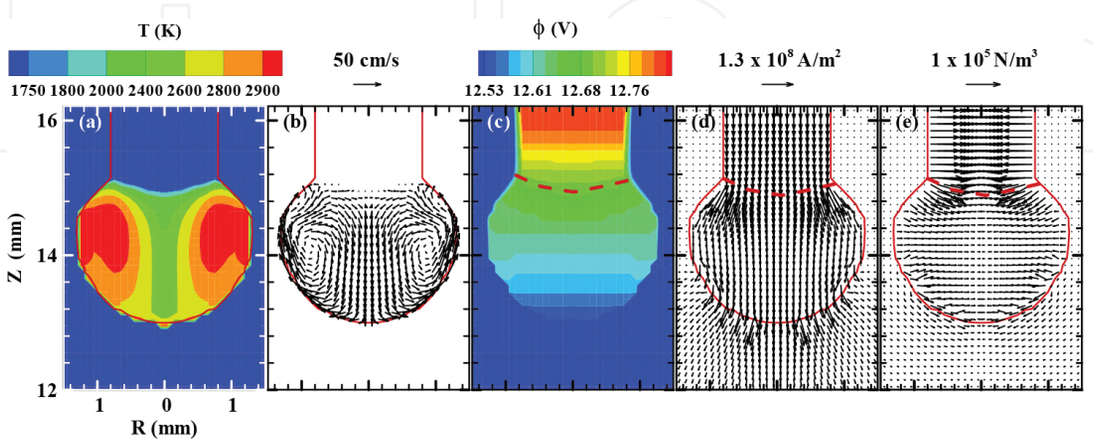

Figure 7. Distribution of physical variables within the droplet at t = 100 ms. (a) Temperature, (b) velocity, (c) electrical potential, (d) current density, and (e) electromagnetic force.

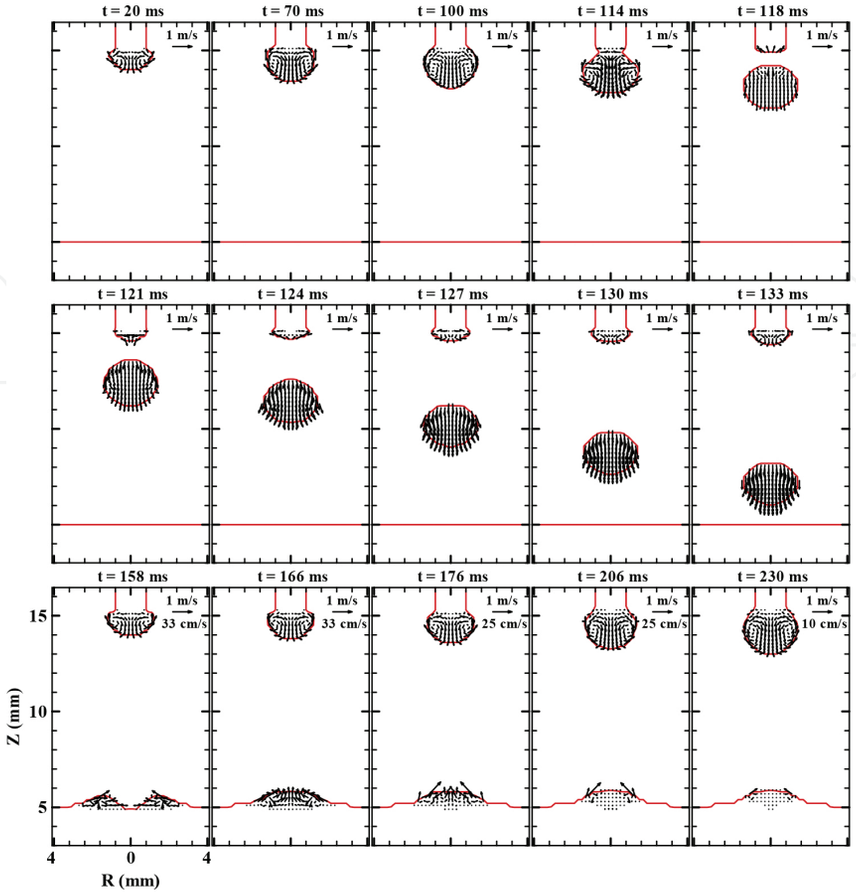

Figure 8. Velocity distributions in the metal showing droplet generation, detachment, transfer in the arc, and impingement onto the weld pool.

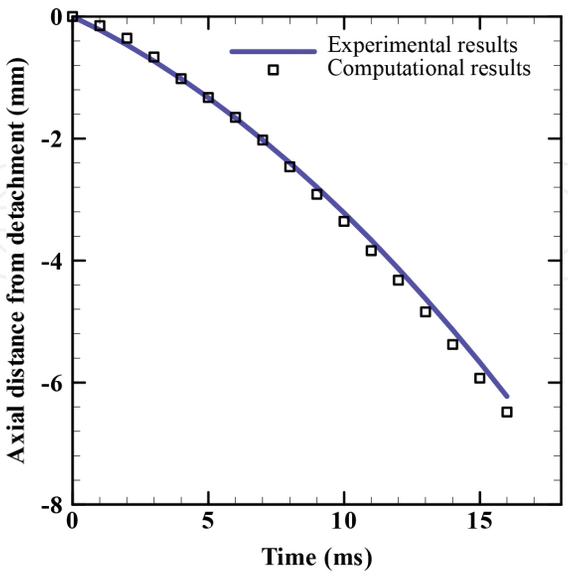

Figure 9. Comparison of droplet flight trajectory with experiment results [32].

http://dx.doi.org/10.5772/64160

The first droplet formation is shown in **Figures 3–5** and **8** from $t = 20$ to 116 ms. A round droplet forms at the electrode tip and grows larger. After a neck is formed at $t = 116$ ms, the velocity within the droplet increases due to the increased electromagnetic pinch force at the neck. After the first droplet is detached at $t = 118$ ms, the second droplet begins to form at the electrode tip. The droplet is detached and transferred to the workpiece from $t = 118$ to 133 ms. The detached droplet is accelerated by the plasma arc and gravity and reaches the workpiece with an axial velocity of about 60 cm/s. The center positions of the first detached droplet shown in **Figure 8** are plotted as a function of time and compared with the flight trajectory taken by Jones et al. [32] in **Figure 9**. The droplet trajectory from the computation matches the experimental results. The droplet acceleration obtained by taking the second derivative of the curve is found to be 24 m/s^2, which is comparable to 21 m/s^2 in [32].

4.3. Weld-pool dynamics and solidification

Figures 3 and **8** show the first droplet impingement onto the workpiece and form a weld pool. The weld pool grows wider and deeper with more droplets deposited into it. The final weld-

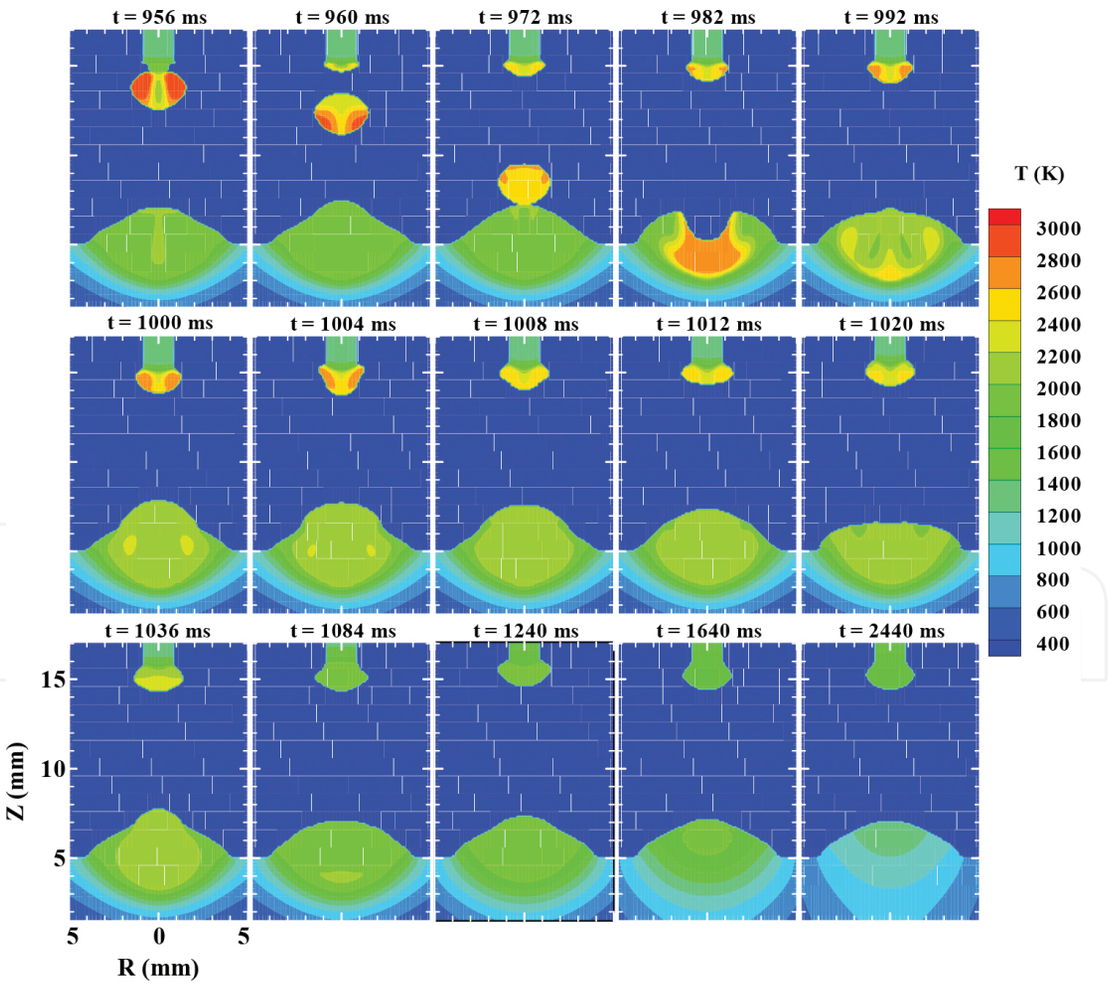

Figure 10. A sequence of temperature distributions in the metal showing droplet generation, detachment, transfer in the arc, impingement onto the weld pool, and weld-pool dynamics.

pool shape and the resulting final weld shape are determined by weld-pool dynamics subject to periodic droplet impingement and several important forces, including electromagnetic force, arc pressure, plasma shear stress, surface tension, and gravity force. As shown in **Figures 10** and **11**, a droplet is ready to be detached from the electrode tip at t = 956 ms. Two vortices formed in the weld pool with an inward flow at the weld-pool surface and a downward flow at the center. The inward flow at the weld-pool surface is driven by the surface tension and the downward flow is mainly by the arc pressure force. When the arc pressure at the weld-pool surface decreases due to a droplet stuck in the arc column, as shown in **Figures 12** and **13**, the fluid at the weld-pool center rises up at t = 960 ms. A crater is formed after a droplet impinges onto the weld pool at t = 982 ms. The high-temperature filler metal carried by the droplet reaches the bottom of the weld pool. The crater is then filled up by the surrounding fluid, and the weld pool first oscillates at high amplitude, then the oscillation gradually subsides. A sequence of experimental images is given in Ref. [43] showing the weld-pool oscillation after a droplet impinges onto the weld pool, which can be seen by the up-and-down movement of the weld-pool surface.

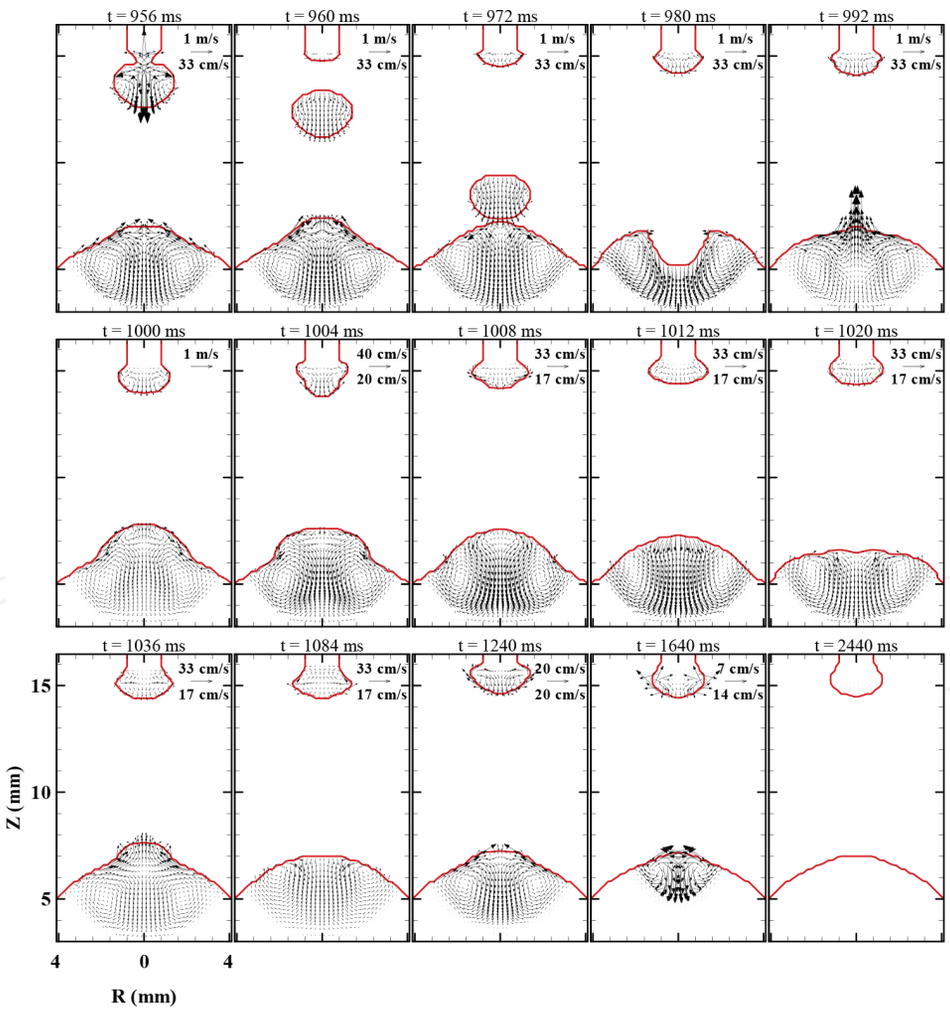

Figure 11. The corresponding velocity distributions of the cases shown in **Figures 10**.

http://dx.doi.org/10.5772/64160

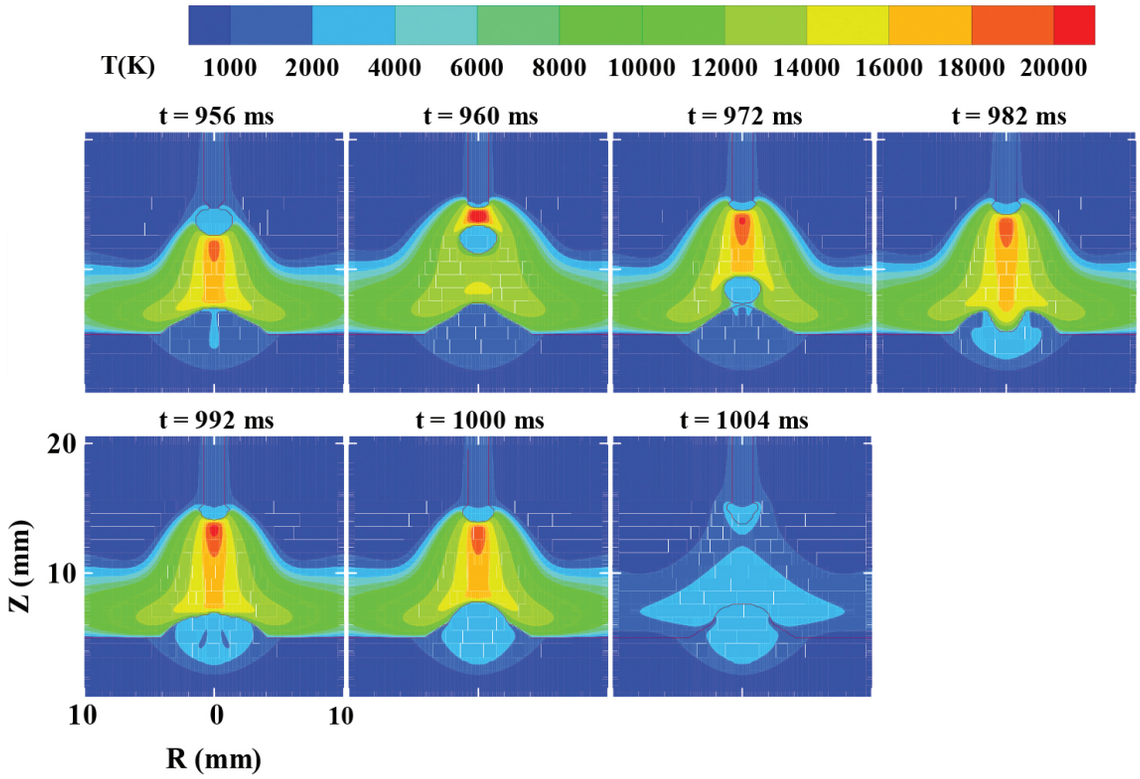

Figure 12. Temperature distributions in the arc plasma during the last droplet impingement and weld-pool dynamics.

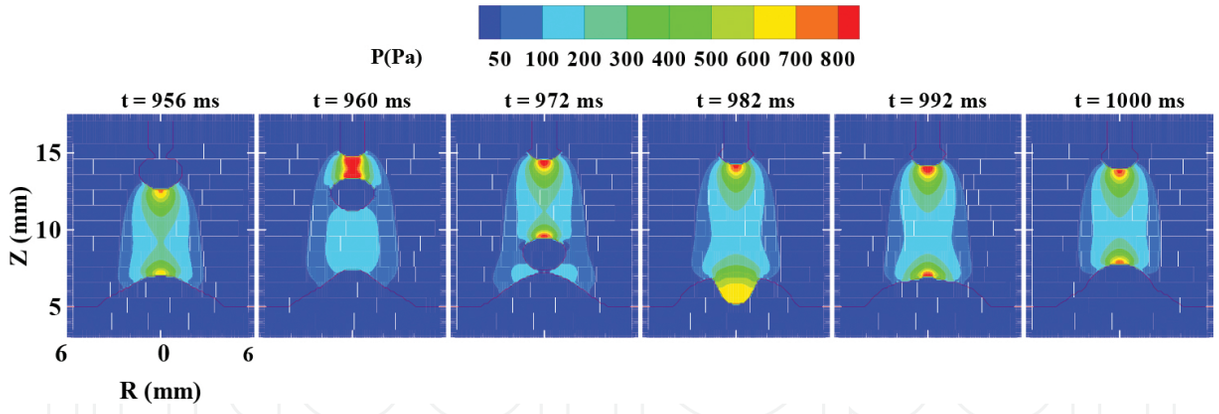

Figure 13. Pressure distributions in the arc plasma during the last droplet impingement and weld-pool dynamics.

At $t = 1000$ ms, the current is turned off and the temperature in the arc plasma decreases rapidly due to the high radiation loss and low heat capacity of the arc plasma. At $t = 1004$ ms, the high-temperature arc plasma is replaced by the nonionized shielding gas, which is continued to protect the solidifying weld pool. After a sudden removal of arc pressure and plasma shear stress at the electrode and weld-pool surfaces, the remnant droplet at the electrode and the weld pool oscillates and the oscillation is balanced by the surface tension. The sizes of the molten droplet and the weld pool become smaller with the heat loss to the solid metal by

conduction and to the surroundings by radiation and convection. As steel is a good thermal conductor, the heat loss occurs mainly through conduction to the solid metal. Therefore, the liquid metal adjacent to the solid and liquid interface solidifies first and the solidus line moves outward toward the electrode and weld-pool surfaces. The solidification completes at t = 2600 ms in the electrode and at t = 2440 ms in the weld pool. **Figure 14** shows the final shape of the weld bead including the weld penetration, which is similar to the reported experimental results [7, 8, 43].

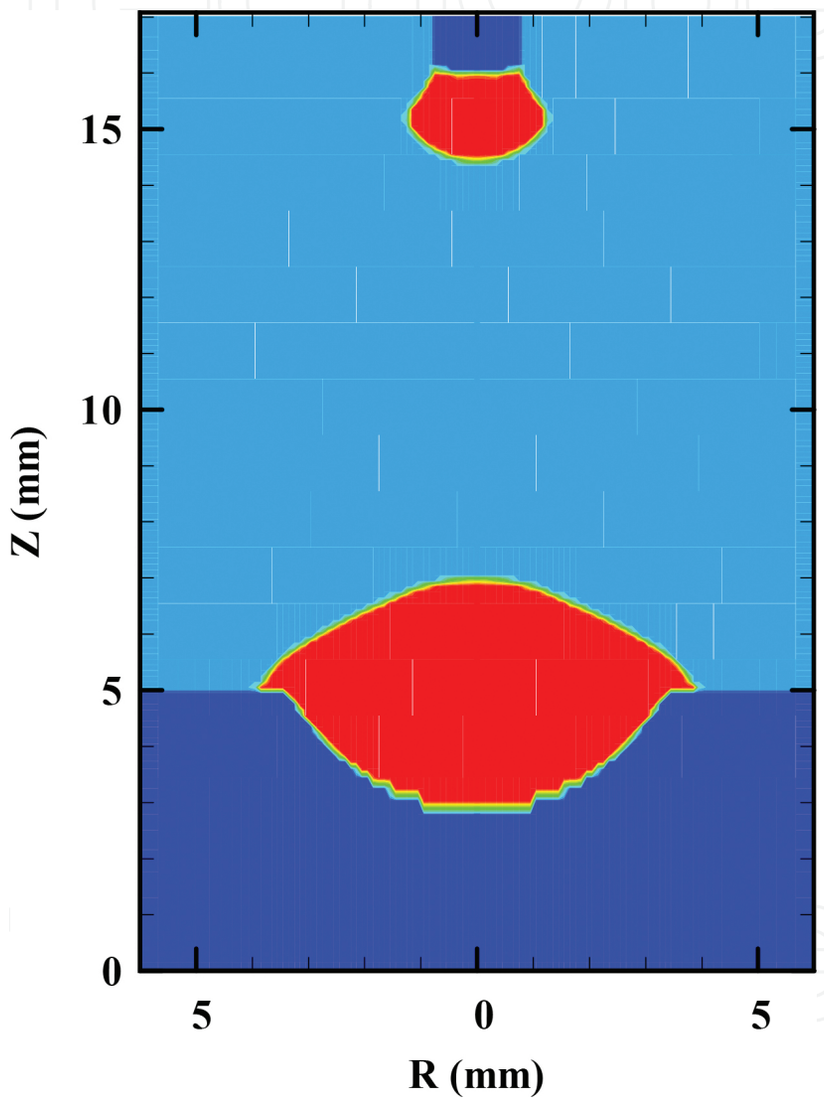

Figure 14. The solidified weld-bead shape.

5. Conclusions

A comprehensive model has been presented to simulate the transport phenomena in a gas metal arc-welding process, including the arc plasma evolution, the melting of the electrode

http://dx.doi.org/10.5772/64160

and the droplet generation, detachment, transfer, and impingement onto the workpiece, and the weld-pool dynamics and solidification. This model included all the three regions—the electrode, the arc plasma, and the weld pool—in the computational domain and modeled the interactive coupling between these three regions. The distributions of arc pressure, current density, and heat flux at the weld-pool surface are found to vary in a wide range, and thus cannot be represented by a fixed distribution in many published GMAW models. The simulation results have revealed physical insights which cannot be found with those isolated single-region models in the literature. The transient evolution of the arc plasma was found to influence and also to be influenced by the droplet formation, detachment, transfer in the arc, and weld-pool dynamics. Therefore, a comprehensive model is required to accurately take into account the coupling events in both the arc domain and metal domain. The comprehensive model can be used to study the effects of process parameters on the welding process and the final weld formation, such as droplet generation with pulse currents to achieve one droplet per pulse (ODPP) and the effects of shielding gas and wire feed rate on the welding process.

Author details

Junling Hu[1*], Zhenghua Rao[2] and Hai-Lung Tsai[3]

*Address all correspondence to: jjhu@bridgeport.edu

1 Department of Mechanical Engineering, University of Bridgeport, Bridgeport, CT, USA

2 School of Energy Science and Engineering, Central South University, Changsha, China

3 Department of Mechanical and Aerospace Engineering, Missouri University of Science and Technology, Rolla, MO, USA

References

[1] Choi S.K., Yoo C.D., Kim Y.-S. The dynamic analysis of metal transfer in pulsed current gas metal arc welding. J. Phys. D: Appl. Phys. 1998; 31: 207–215.

[2] Choi S.K., Yoo C.D., Kim Y.-S. Dynamic simulation of metal transfer in GMAW, Part 1: globular and spray transfer mode. Weld. J. 1998: 38–44s.

[3] Choi S.K., Yoo C.D., Kim Y.-S. Dynamic simulation of metal transfer in GMAW, Part 2: short-circuit transfer mode. Weld. J. 1998: 45–51s.

[4] Wang G., Huang P.G., Zhang Y.M. Numerical analysis of metal transfer in gas metal arc welding. Metall. Trans. 2003; 34B: 345–353.

[5] Wang G., Huang P.G., Zhang Y.M. Numerical analysis of metal transfer in gas metal arc welding under modified pulsed current conditions. Metall. Trans. 2004; 35B(5): 857–866.

[6] Wang F., Hou W.K., Hu S.J., Kannatey-Asibu E., Schultz W.W., Wang P.C. Modelling and analysis of metal transfer in gas metal arc welding. J. Phys. D: Appl. Phys. 2003; 36: 1143–1152.

[7] Fan H.G., Kovacevic R. Droplet formation, detachment, and impingement on the molten pool in gas metal arc welding. Metall. Trans. 1999; 30B: 791–801.

[8] Fan H.G., Kovacevic R. Dynamic analysis of globular metal transfer in gas metal arc welding – a comparison of numerical and experimental results. J. Phys. D: Appl. Phys. 1998; 31: 2929–2941.

[9] Tsao K.C., Wu C.S. Fluid flow and heat transfer in GMA weld pools. Weld. J. 1988; 70–75s.

[10] Kumar S., Bhaduri S.C. Three-dimensional finite element modeling of gas metal-arc welding. Metall. Trans. 1994; 25B: 435–441.

[11] Kumar S., Bhaduri S.C. Theoretical investigation of penetration characteristics in gas metal-arc welding using finite element method. Metall. Trans. 1994; 26B: 611–624.

[12] Jaidi J., Dutta P. Modeling of transport phenomena in a gas metal arc welding process. Numer. Heat Transf. A. 2001; 40: 543–562.

[13] Kim J.-W., Na S.-J. A study on the effect of constant tube-to-workpiece distance on weld pool shape in gas metal arc welding. Weld. J. 1995; 74(5): 141–152s.

[14] Ohring S., Lugt H.J. Numerical simulation of a time-dependent 3-D GMA weld pool due to a moving arc. Weld. J. 1999: 416–424s.

[15] Kim C.-H., Zhang W., DebRoy T. Modeling of temperature field and solidified surface profile during gas-metal arc fillet welding. J. Appl. Phys. 2003; 94: 2667–2679.

[16] Kim W.H., Fan H.G., Na S.J. Effect of various driving forces on heat and mass transfer in arc welding. Numer. Heat Transf. A. 1997; 32(6): 633–652.

[17] Chen J., Schwenk C., Wu C. S., Rethmeier M. Predicting the influence of groove angle on heat transfer and fluid flow for new gas metal arc welding processes. Int. J. Heat Mass Transf. 2012; 55(1–3): 102–111.

[18] Cheon J., Kiran D.V., Na S.-J. CFD based visualization of the finger shaped evolution in the gas metal arc welding process. Int. J. Heat Mass Transf. 2016; 97: 1–14.

[19] Jia X., Xu J., Liu Z., Huang, S., Fan Y., Sun Z. A new method to estimate heat source parameters in gas metal arc welding simulation process. Fusion Eng. Des. 2014; 89(1): 40–48.

[20] Cao Z., Yang Z., Chen X.L. Three-dimensional simulation of transient GMA weld pool with free surface. Weld. J. 2004: 169–176s.

[21] Wang Y., Tsai H.L. Impingement of filler droplets and weld pool dynamics during gas metal arc welding process. Int. J. Heat Mass Transf. 2001; 44: 2067–2080.

[22] Wang Y., Shi Q., Tsai H.L. Modeling of the effects of surface-active elements on flow patterns and weld penetration. Metall. Trans. 2001; 32B: 145–161.

[23] Wang Y., Tsai H.L. Effects of surface active elements on weld pool fluid flow and weld penetration in gas metal arc welding. Metall. Trans. 2001; 32B: 501–515.

[24] Guo H., Hu J., Tsai H.L. Three-dimensional modeling of gas metal arc welding of aluminum alloys. J. Manuf. Sci. Eng. 2010; 132: 021011.

[25] Guo H., Hu J., Tsai H.L. Numerical modeling of cold weld formation and improvement in GMAW of aluminum alloys. Numer. Heat Transf. Part A: Appl. 2010; 57: 392–414.

[26] Guo H., Hu J., Tsai H.L. Formation of weld crater in GMAW of aluminum alloys. Int. J. Heat Mass Transf. 2009; 52: 5533–5546.

[27] Hu J., Tsai H.L. Modeling of transport phenomena in 3D GMAW of thick metal with V-groove. J. Phys. D: Appl. Phys. 2008; 41: 065202.

[28] Hu J., Guo H., Tsai H.L. Weld pool dynamics and the formation of ripples in 3D gas metal arc welding. Int. J. Heat Mass Transf. 2008; 51: 2537–2552.

[29] Wu L., Cheon J., Kiran D.V., Na S.-J. CFD simulations of GMA welding of horizontal fillet joints based on coordinate rotation of arc models. J. Mater. Process. Technol. 2016; 231: 221–238.

[30] Jones L.A., Eagar T.W., Lang J.H. Images of steel electrode in Ar-2%O_2 shielding during constant current gas metal arc welding. Weld. J. 1998: 135–141s.

[31] Jones L.A., Eagar T.W., Lang J.H. Magnetic forces acting on molten drops in gas metal arc welding. J. Phys. D: Appl. Phys. 1998; 31: 93–106.

[32] Jones L.A., Eagar T.W., Lang J.H. A dynamic model of drops detaching from a gas metal arc welding electrode. J. Phys. D: Appl. Phys. 1998; 31: 107–123.

[33] Haidar J. A theoretical model for gas metal arc welding and gas tungsten arc welding. I. J. Appl. Phys. 1998; 84(7): 3518–3529.

[34] Haidar J., Lowke J.J. Predictions of metal droplet formation in arc welding. J. Appl. Phys. D: Appl. Phys. 1996; 29: 2951–2960.

[35] Haidar J. An analysis of the formation of metal droplets in arc welding. J. Phys. D: Appl. Phys. 1998; 31: 1233–1244.

[36] Haidar J. Prediction of metal droplet formation in gas metal arc welding. II. J. Appl. Phys. 1998; 84(7): 3530–3540.

[37] Haidar J. An analysis of heat transfer and fume production in gas metal arc welding. III. J. Appl. Phys. 1998; 85(7): 3448–3459.

[38] Hertel, M., Spille-Kohoff A., Füssel U., Schnicket M. Numerical simulation of droplet detachment in pulsed gas–metal arc welding including the influence of metal vapour. J. Phys. D: Appl. Phys. 2013; 46(22): 224003.

[39] Schnick, M., Fuessel U., Hertel M., Haessler M., Spille-Kohoff A., Murphy A.B. Modelling of gas–metal arc welding taking into account metal vapour. J. Phys. D: Appl. Phys. 2010; 43(43): 434008.

[40] Murphy A.B. Why the arc, and its interactions with the electrodes, are important in predictive modelling of arc welding. Plasma Phys. Technol. 2015; 2: 233–240.

[41] Murphy A.B. A self-consistent three-dimensional model of the arc, electrode and weld pool in gas–metal arc welding. J. Phys. D: Appl. Phys. 2011; 44(19): 194009.

[42] Lu F., Wang H.-P., Murphy A.B., Carlson B.E. Analysis of energy flow in gas metal arc welding processes through self-consistent three-dimensional process simulation. Int. J. Heat Mass Transf. 2014; 68: 215–223.

[43] Fan H.G., Kovacevic R. A unified model of transport phenomena in gas metal arc welding including electrode, arc plasma and molten pool. J. Phys. D: Appl. Phys. 2004; 37: 2531–2544.

[44] Hu J., Tsai H.L. Heat and mass transfer in gas metal arc welding, Part I: the arc. Int. J. Heat Mass Transf. 2007; 50: 833–846.

[45] Hu J., Tsai H.L. Heat and mass transfer in gas metal arc welding, Part II: the metal. Int. J. Heat Mass Transf. 2007; 50: 808–820.

[46] Hu J., Tsai H.L. Effects of welding current on droplet generation and arc plasma in gas metal arc welding. J. Appl. Phys. 2006; 100: 053304.

[47] Hu J., Tsai H.L. Metal transfer and arc plasma in gas metal arc welding. J. Heat Transf. 2007; 129: 1025–1035.

[48] Xu G., Hu J., Tsai H.L. Three-dimensional modeling of arc plasma and metal transfer in gas metal arc welding. Int. J. Heat Mass Transf. 2009; 52: 1709–1724.

[49] Rao Z.H., Hu J., Liao S.M., Tsai H.L. Modeling of the transport phenomena in GMAW using argon-helium mixtures, Part I – the arc. Int. J. Heat Mass Transf. 2010; 53: 5722–5732.

[50] Rao Z.H., Hu J., Liao S.M., Tsai H.L. Modeling of the transport phenomena in GMAW using argon-helium mixtures, Part II – the metal. Int. J. Heat Mass Transf. 2010; 53: 5707–5721.

[51] Rao Z.H., Liao S.M., Tsai H.L. Effects of shielding gas compositions on arc plasma and metal transfer in gas metal arc welding. J. Appl. Phys. 2010; 107(4): 044902.

[52] Rao Z.H., Zhou J., Tsai H.L. Determination of equilibrium wire-feed-speeds for stable gas metal arc welding. Int. J. Heat Mass Transf. 2012; 55(23–24): 6651–6664.

[53] Diao Q.Z., Tsai H.L. Modeling of solute redistribution in the mushy zone during solidification of aluminum-copper alloys. Metall. Trans. 1993; 24A: 963–973.

[54] Carman P.C. Fluid flow through granular beds. Trans. Inst. Chem. Eng. 1937; 15: 150–166.

[55] Kubo K., Pehlke R.D. Mathematical modeling of porosity formation in solidification. Metall. Trans. 1985; 16A: 823–829.

[56] Beavers G.S., Sparrow E.M. Non-Darcy flow through fibrous porous media. J. Appl. Mech. 1969; 36: 711–714.

[57] Lowke J.J., Kovitya P., Schmidt H.P. Theory of free-burning arc columns including the influence of the cathode. J. Phys. D: Appl. Phys. 1992; 25:1600–1606.

[58] Lancaster J.F. The physics of welding. 2nd ed. Oxford: Pergamon Press; 1986.

[59] Torrey M.D., Cloutman L.D., Mjolsness R.C., Hirt C.W. NASA-VOF2D: a computer program for incompressible flows with free surfaces. LA-10612-MS. Los Alamos National Laboratory; 1985.

[60] Brackbill J.U., Kothe D.B., Zemach C. A continuum method for modeling surface tension. J. Comput. Phys. 1992; 100: 335–354.

[61] Celic A., Zilliac G.G. Computational study of surface tension and wall adhesion effects on an oil film flow underneath an air boundary layer. NASA Ames Research Center; August 1997.

[62] Finkelnburg W., Segal S.M. The potential field in and around a gas discharge, and its influence on the discharge mechanism. Phys. Rev. Lett. 1951; 83: 582–585.

[63] Zacharia T., David S.A., Vitek J.M. Effect of evaporation and temperature-dependent material properties on weld pool development. Metall. Trans. 1992; 22B: 233–241.

[64] Granger R.A. Fluid mechanics. New York: CBS College; 1985.

[65] Patanka S.V. Numerical heat transfer and fluid flow. New York: McGraw-Hill; 1980.

IntechOpen

IntechOpen